IET Journals
The Institution of Engineering and Technology

A Multi-Antenna Super-Resolution Passive Wi-Fi Radar Algorithm: Combined Model Order Selection and Parameter Estimation

ISSN 1751-8644
doi: 0000000000
www.ietdl.org

Hasan Can Yildirim[1,2] *Laurent Storrer*[1] *Philippe De Doncker*[1] *Jerôme Louveaux*[2] *François Horlin*[1]

[1] *OPERA - WCG, Université Libre de Bruxelles, Brussels, Belgium*
[2] *ICTM - ELEN, Université Catholique de Louvain, Louvain-la-neuve, Belgium*
** E-mail: hasan.can.yildirim@ulb.be*

Abstract: In recent years, Wi-Fi has become the main gateway that connects users to the internet. Considering the availability of Wi-Fi signals, and their suitability for channel estimation, IEEE established the Wi-Fi Sensing (WS) Task Group whose purpose is to study the feasibility of Wi-Fi-based environment sensing. However, Wi-Fi signals are transmitted over limited bandwidths with a relatively small number of antennas in bursts, fundamentally limiting the range, Angle-of-Arrival and speed resolutions. This paper presents a super-resolution algorithm to perform the parameter estimation in a quasi-monostatic WS scenario. The proposed algorithm, RIVES, estimates the range, Angle-of-Arrival and speed parameters with Vandermonde decomposition of Hankel matrices. To estimate the size of the signal subspace, RIVES uses a novel Model Order Selection method which eliminates spurious noise targets based on their distance to the noise and signal subspaces. Various scenarios with multiple targets are simulated to show the robustness of RIVES. In order to prove its accuracy, real-life indoor experiments are conducted with human targets by using Software Defined Radios.

1 Introduction

In the past 20 years, Wi-Fi technologies have evolved to satisfy the high throughput demands in a wide variety of scenarios where tens of devices can be connected to a single Wi-Fi Access Point (AP). In order to achieve the required throughputs, the Wi-Fi standard (IEEE 802.11) has been ever-evolving. The most recent Wi-Fi standard, namely 802.11be, will bring even wider bandwidths (up to 320 MHz), enhanced spatial diversity (maximum of 16 spatial streams), and possibly, coordinated and joint transmission by multiple APs.

In the meantime, wireless channel sensing, and its related applications, attracted the attention of the academy and the industry. The goal in wireless channel sensing is to detect and track humans and/or other objects by applying radar processing schemes [1] [2] [3]. Recently, IEEE established the Wi-Fi Sensing (WS) Task Group 802.11bf [4] whose purpose is to study the feasibility and reliability of Wi-Fi-based environment sensing within the IEEE 802.11 framework. However, specifically for human movement detection/tracking, the following fundamental limitations bring new challenges [5]:

- Range resolution, which is limited by the signal bandwidth. Clearly, WS will make use of the increased signal bandwidth in 11be, providing roughly 0.5 meters range resolution. However, considering the fact that indoor Channel Impulse Responses (CIRs) are very rich in terms of multipath components (MPCs), even better range resolutions are needed for reliable estimation [6], [7], [8].
- Angle-of-Arrival (AoA) resolution, which is limited by the number of antennas. Most of the modern communication and radar systems use super-resolution methods for AoA estimation. However, regardless of the algorithm, increasing the number of available antennas increases the spatial resolution, as well as the complexity and the cost of such a system.
- Speed resolution, which is limited by the duration of the available signal. Wi-Fi signals are transmitted in bursts and often interrupted by other signals [9]: i) the transmission of acknowledgments; ii) the interfering signals from other cells, and iii) synchronization frames used for Multi-User Multiple-Input Multiple-Output and Orthogonal Frequency Division Multiple Access technologies. Furthermore, higher modulation orders are introduced (up to 1024 QAM). Hence, an equal amount of data can be transmitted over a shorter frame duration compared to the previous versions of the standard, which further limits the available signal duration. Therefore, the duration of Wi-Fi bursts is not long enough to achieve the desired speed resolution for human movement detection.

These three fundamental problems on the range, AoA and speed estimation have been discussed within the WS Task Group. To cope with the low estimation accuracy of FFT-based processing, various subspace-based super-resolution algorithms have been proposed in the literature. In summary, subspace-based parametric estimation methods are designed to provide better resolution than the FFT-based non-parametric methods [10]. However, to achieve such resolutions, the size of the signal subspace has to be estimated, also known as the Model Order Selection (MOS). Thus, the reliability of the entire system depends on both the accuracy of the spectral parameter estimation, as well as the accuracy of the MOS method.

In [11], MUSIC algorithm is introduced where the frequency content of the sample covariance matrix (SCM) is estimated by exploiting the orthogonality between signal and noise subspaces. In [12], the foundation of ESPRIT algorithm is given for one-dimensional (1D) parameter estimation which exploits the rotational invariance present in the eigenvectors of SCM. The parameter estimation performance of ESPRIT is relatively poor in low signal-to-noise-power-ratio (SNR) conditions compared to MUSIC [13]. However, MUSIC needs spectral peak searching which increases its computational complexity. In the context of radar-like parameter estimation with ESPRIT, the literature is extensive. In [14], the range and Doppler frequencies are estimated with ESPRIT and Least Square (LS) algorithms, by exploiting the unique Orthogonal Frequency Division Multiplexing (OFDM) frame structure of Radar-Communications systems. However, the algorithms are optimized for high target velocities such as 80 and 100 km/h, which already yield very high Doppler frequencies. In [15], the range and speed estimation is performed with ESPRIT by considering 802.11p signals. The integration time is considered to be around 50ms, which is not realistic for Wi-Fi signals. In reality, the Wi-Fi bursts are much shorter yielding only a few milliseconds of integration time (if the

channel coherence time is sufficiently high). Since data transfer is often interrupted by management/control frames and Wi-Fi is a system that provides data transfer only by request, such low integration times are introduce a problem for Doppler resolution. Moreover, in both of these works, the number of targets is assumed to be known. In other words, no MOS algorithm is implemented.

The size of the signal subspace, i.e, the number of paths or targets in the environment, is required in order to guarantee a robust parameter estimation with subspace-based super-resolution algorithms. If the true size of the signal subspace is not correctly estimated, there will be either misdetections or false alarms [16]. Various MOS methods exist in the literature to estimate the size of the signal subspace (see [17], [18] and the references therein). More recently in [19], it is proven that the distribution of the eigenvalues in the SCM cannot be considered as a reliable criterion when SNR is relatively low. In [20] (ESTER), ESPRIT algorithm is used to estimate the spectral parameters with an erroneous model for MOS. Then, the residual perturbation errors are minimized to correct the errors made during the MOS stage. In [21] (SAMOS), subspace shift-invariance characteristic of the SCM is exploited to estimate the model order of the system. However, MOS accuracy of ESTER and SAMOS decreases as the number of sources increases. From the radar point-of-view, this intrinsically means that ESTER or SAMOS reliably work only if the number of targets is low. Therefore, the existing MOS methods do not perform well in indoor radar-like scenarios since the number of MPCs can be very large). Furthermore, the existing methods are designed to only estimate the model order of a system, without taking care of the spectral parameter estimation after the MOS stage.

We have proposed a preliminary radar architecture for indoor human/object detection and tracking [22]. However, the radar architecture was limited by: i) only the range and speed estimations; ii) the estimation of signal and noise subspaces through the sample covariance matrix, which incurs a potential loss of information due to the phase terms that cancel/affect each other, and iii) serialized implementation of the proposed architecture. To deal with these shortcomings, we propose a new subspace-based super-resolution parameter estimation architecture, namely Recursive Isolation of Vandermonde-like Eigen-Spaces (RIVES) which is capable of estimating the range, AoA and speed of multiple objects. RIVES combines a novel MOS method and the ESPRIT algorithm to reach the desired estimation accuracy for indoor human target detection and tracking. RIVES is designed to first estimate the spectral parameters for an over-sized signal subspace spanned by the sample Hankel matrix. Then, the corresponding over-sized Vandermonde matrix is constructed, whose columns span the entire signal subspace as well as a part of the noise subspace [23]. The estimated parameters are refined in the MOS stage by exploiting the orthogonality between signal and noise subspaces [11]. Therefore, different sets of eigenvectors that span the row and column spaces of the Hankel matrix are efficiently combined for successive parameter and MOS estimation. Finally, the accuracy of RIVES is experimentally validated by using Software-Defined-Radio (SDR)-based multi-antenna prototype. Specifically, USRP X310s are used to emulate an AP and a multi-antenna passive radar/sensing device in an indoor scenario with human targets.

This paper is structured as follows. In section 2, the radar/sensing system model is given for a Single-Input Multiple-Output (SIMO) scenario. In section 3, the generic version of RIVES is explained in detail. In section 4, radar processing with RIVES is shown for range, AoA and speed estimation, respectively. In section 5, the robustness of the novel MOS method and the overall accuracy of RIVES are studied by simulations. In section 6, analyses based on real-life measurements are provided, and the efficiency of RIVES is experimentally validated. Finally, in section 7, the conclusion is drawn.

The notations used throughout this work are summarized in Table 1. Additionally, Q, M, N and P represent the number of OFDM subcarriers, received OFDM symbols,antennas at the receiver and propagation paths, respectively. To improve the readability throughout the paper, the cisoid function is defined as

$$\omega(x) = \exp(-j2\pi x).$$

Table 1 Summary of the mathematical notations

Symbol	Definition	Symbol	Definition
u	Scalar		
$\mathbf{u}$	Vector	u_i	ith entry in $\mathbf{u}$
$\mathbf{U}$	Matrix	$U_{i,j}$	entry of $\mathbf{U}$ at the ith row and jth column
$\hat{u}$	Estimated scalar	$\tilde{u}$	Post-decision scalar
$\hat{\mathbf{u}}$	Estimated vector	$\tilde{\mathbf{u}}$	Post-decision vector
$\hat{\mathbf{U}}$	Estimated matrix	$\tilde{\mathbf{U}}$	Post-decision matrix
$\mathbf{U}(m)$	Matrix $\mathbf{U}$ is a function of scalar m		
$\mathbf{U}^T, \mathbf{U}^*$	Transpose and Hermitian transpose of $\mathbf{U}$		
$\mathbf{U}^+$	Moore-Penrose inverse of $\mathbf{U}$		
$\mathbf{u}[k_1{:}k_2]$	Subvector of $\mathbf{u}$ composed of the entries between indices k_1 and k_2		
$\mathbf{U}[:, k_1{:}k_2]$	Submatrix of $\mathbf{U}$ composed of columns between indices k_1 and k_2		
$\hat{\mathbf{u}}^{(v_i)}$	Vector $\hat{\mathbf{u}}$ is estimated for the ith entry in $\mathbf{v}$		

2 System Model

In this section, we introduce the system model of the Channel Transfer Function (CTF). Although the proposed algorithm can be applied to bistatic or multistatic geometries, we focus on quasi-monostatic geometry where the transmitter (Tx) and the receiver (Rx) are closely located. Moreover, the receiver has access to the transmitted signal and it is equipped with N antennas configured in a Uniform Linear Array (ULA). Since WS is the main focus of this work, the signal model is written only for OFDM signals. However, the model can be extended to more traditional radar/sensing signals such as Frequency Modulated Continuous Wave [24] and Pulse Modulated Continuous Wave [25] [26], as well as the bistatic radar geometry.

2.1 Estimated CTF at any time instant

In order to save space, and focus on more important parts of the system model, we assume that the received OFDM signals already went through the following process: i) correlation is applied to the Short Training Fields to find the starting time of the received OFDM frames; ii) Carrier Frequency Offset is estimated from the High-Efficiency Long Training Fields and compensated accordingly; iii) Cyclic Prefix samples are dropped, and the Fast Fourier Transform (FFT) of each OFDM symbol is computed; iv) through zero-forcing, the CTF is estimated [27] [28], which can be written as

$$\hat{H}[q,n,m] = \sum_{p=1}^{P} \Big(\alpha_p \, \omega\big(\frac{q\tau_p}{QT}\big) \, \omega\big(n\sin(\theta_p)\big) \, \omega\big(f_p m T_f\big) + z[q,n,m] \Big) \quad (1)$$

with $q = 0 \dots Q-1, n = 0 \dots N-1, m = 0 \dots M-1$. The first term models the attenuation due to radio wave propagation. The first cisoid models the effect of the propagation delay τ_p, on subcarrier q, with a normalization factor corresponding to the sampling duration at Rx T. The second cisoid models the phase due to the AoA θ_p, which evolves among N antennas separated by $\lambda_c/2$ distance, where λ_c is the carrier wavelength. The third cisoid models the Doppler frequency shift f_p, that evolves over the slow-time index m and the slow-time sampling rate T_f. Finally, $z[q,n,m]$ corresponds to the Additive White Gaussian Noise (AWGN) samples at subcarrier q, antenna n and slow-time index m.

2.2 Equivalent matrix model

Since the three cisoids model the three orthogonal spaces, namely range, AoA, and speed, one can write (1) in matrix form. To do so, let us introduce the following matrices. The first cisoid can be written

as the delay matrix

$$\boldsymbol{D} = \begin{pmatrix} 1 & \dots & 1 \\ \omega(\frac{1}{QT}\tau_1) & \dots & \omega(\frac{1}{QT}\tau_P) \\ \vdots & \ddots & \vdots \\ \omega(\frac{Q-1}{QT}\tau_1) & \dots & \omega(\frac{Q-1}{QT}\tau_P) \end{pmatrix} \in \mathbb{C}^{Q\times P} \quad (2)$$

whose rows correspond to different subcarriers. The second cisoid can be written as the AoA matrix

$$\boldsymbol{\Theta} = \begin{pmatrix} 1 & \dots & 1 \\ \omega(\frac{1}{2}\sin(\theta_1)) & \dots & \omega(\frac{1}{2}\sin(\theta_P)) \\ \vdots & \ddots & \vdots \\ \omega(\frac{N-1}{2}\sin(\theta_1)) & \dots & \omega(\frac{N-1}{2}\sin(\theta_P)) \end{pmatrix} \in \mathbb{C}^{N\times P} \quad (3)$$

whose rows correspond to different antennas. Furthermore, the columns of $\mathbf{D}$ and $\boldsymbol{\Theta}$ identify different propagation path delays and AoA angles, respectively. The diagonal matrix $\boldsymbol{A}(m) \in \mathbb{C}^{P\times P}$ whose entries correspond to the path attenuations and the Doppler phases at slow-time instant m can be written as

$$\boldsymbol{A}(m) = \begin{pmatrix} \alpha_1\omega(mf_1T_f) & 0 & \dots & 0 \\ 0 & \alpha_2\omega(mf_2T_f) & \dots & 0 \\ \vdots & \vdots & \ddots & \vdots \\ 0 & 0 & \dots & \alpha_P\omega(mf_PT_f) \end{pmatrix}. \quad (4)$$

Finally, (1) can be written in matrix form

$$\begin{aligned} \hat{\mathbf{H}}(m) &= \mathbf{D}\ \mathbf{A}(m)\ \boldsymbol{\Theta}^T + \mathbf{Z}(m), \in \mathbb{C}^{Q\times N} \\ &= \begin{pmatrix} H[0,0,m] & \dots & H[0,N{-}1,m] \\ \vdots & \ddots & \vdots \\ H[Q{-}1,0,m] & \dots & H[Q-1,N{-}1,m] \end{pmatrix} + \mathbf{Z}(m). \end{aligned} \quad (5)$$

Here, $\hat{\mathbf{H}}(m) \in \mathbb{C}^{Q\times N}$ is written as a function of the slow-time index m. Each column of $\hat{\mathbf{H}}(m)$ contains the CTF estimated at antenna n, while its rows correspond to the different subcarriers q. Moreover, $\mathbf{Z}(m) \in \mathbb{C}^{Q\times N}$ is the noise matrix whose entries are the samples of $z[q,n,m]$ given in (1).

3 Super-Resolution Parameter Estimation: Recursive Isolation of Vandermonde-like Eigenspaces

In this section, we introduce the RIVES algorithm to estimate the entries of a vector $\boldsymbol{\mu} \in \mathbb{R}^L$ whose entries define the following Vandermonde matrix

$$\mathbf{V} = \begin{pmatrix} 1 & \dots & 1 \\ \omega(\mu_1\eta) & \dots & \omega(\mu_L\eta) \\ \vdots & \ddots & \vdots \\ \omega((K_1-1)\mu_1\eta) & \dots & \omega((K_1-1)\mu_L\eta) \end{pmatrix} \in \mathbb{C}^{K_1\times L} \quad (6)$$

where K_1 and K_2 correspond to the size of the measurement dimensions, e.g., the number of subcarriers and antennas, and η corresponds to a generic normalization factor. RIVES can be applied to any linear system of the form

$$\hat{\mathbf{Y}} = \mathbf{VB} + \mathbf{Z}, \in \mathbb{C}^{K_1\times K_2} \quad (7)$$

where $\mathbf{B}$ is the source matrix of arbitrary size, i.e., it can be a single row vector or a matrix, $\mathbf{Z}$ is the matrix whose entries are the AWGN noise samples. RIVES can estimate the size of the vector $\boldsymbol{\mu} \in \mathbb{R}^L$, i.e., $\hat{L}$, as well as its entries corresponding to the parameters-of-interest, from the measurement matrix $\mathbf{Y}$, without any knowledge about the source matrix $\mathbf{B}$. To do so, the measurement matrix goes through two subsequent stages in RIVES. In the first stage, the parameters-of-interest are estimated for an oversized $\mathbf{V}$ since the number of resolvable paths is not known a priori. In other words, since the true size of $\boldsymbol{\mu}$ is not known, $\hat{\boldsymbol{\mu}} \in \mathbb{R}^{L_o}$ is obtained where $L_o{>}L$ is guaranteed. This process is explained in Section 3.1. In the second stage, a novel MOS method is proposed to separate the real parameters from spurious noise parameters. The entries in $\hat{\boldsymbol{\mu}}$ are tested against a threshold to decide whether a given entry corresponds to a real parameter or a spurious noise parameter. This process is explained in Section 3.2. Finally, there are three inputs to the algorithm; i) the measurement matrix $\mathbf{Y}$; ii) the maximum expected size of the signal subspace L_o, and iii) the normalization parameter η.

3.1 Estimation Stage

Before we apply the ESPRIT algorithm for parameter estimation, let us define the Hankel matrix as follows

$$\boldsymbol{\mathcal{H}}(k_2) = \begin{pmatrix} \hat{Y}_{1,k_2} & \hat{Y}_{2,k_2} & \dots & \hat{Y}_{\frac{K_1}{2},k_2} \\ \hat{Y}_{2,k_2} & \hat{Y}_{3,k_2} & \dots & \hat{Y}_{\frac{K_1}{2}+1,k_2} \\ \vdots & \vdots & \ddots & \vdots \\ \hat{Y}_{\frac{K_1}{2},k_2} & \hat{Y}_{\frac{K_1}{2}+1,k_2} & \dots & \hat{Y}_{K_1,k_2} \end{pmatrix}, \in \mathbb{C}^{\frac{K_1}{2}\times\frac{K_1}{2}}$$

where $k_2 = 1,\dots,K_2$. The first row and first column of $\boldsymbol{\mathcal{H}}(k_2)$ are identical, and its entries are symmetric along the diagonal, i.e., constant skew diagonals. The structure of the Hankel matrix is very suitable for subspace-based parameter estimation since its eigenvalue decomposition yields a Vandermonde matrix spanning the signal and noise subspaces of the parent matrix [29] [30]. Moreover, Hankel matrices do not require spatial smoothing as opposed to the SCMs, which smoothens the transition between the eigenvalues and makes the estimation of the size of subspaces much more difficult [31] [32]. Moreover, when K_2 measurements are available, the block Hankel matrix can be constructed to improve the SNR and reduce the risk of destructive interference among different measurements, which is defined as

$$\boldsymbol{\mathcal{H}} = \begin{pmatrix} \boldsymbol{\mathcal{H}}(1) & \boldsymbol{\mathcal{H}}(2) & \dots & \boldsymbol{\mathcal{H}}(\frac{K_2}{2}) \\ \boldsymbol{\mathcal{H}}(2) & \boldsymbol{\mathcal{H}}(2) & \dots & \boldsymbol{\mathcal{H}}(\frac{K_2}{2}+1) \\ \vdots & \vdots & \ddots & \vdots \\ \boldsymbol{\mathcal{H}}(\frac{K_2}{2}) & \boldsymbol{\mathcal{H}}(\frac{K_2}{2}+1) & \dots & \boldsymbol{\mathcal{H}}(K_2) \end{pmatrix} \quad (8)$$

where $\boldsymbol{\mathcal{H}} \in \mathbb{C}^{K_3\times K_3}$ and $K_3 = \frac{K_1K_2}{4}$. Here, the structure of the block Hankel matrix is adjusted in such a way that its eigenvalue decomposition is equivalent to its Vandermonde factorization [23], which can defined as

$$\boldsymbol{\mathcal{H}} = \mathbf{U}\boldsymbol{\Sigma}\boldsymbol{\mathcal{V}}^T \quad (9)$$

where the rows of $\boldsymbol{\mathcal{V}}^T$ are the right singular vectors. The columns of $\mathbf{U}$ correspond to the basis vectors of signal and noise subspaces, and the diagonal entries of $\boldsymbol{\Sigma}$ are the associated eigenvalues. The estimation stage is finalized by applying ESPRIT on the first L_o columns of $\mathbf{U}$, such as

$$\hat{\boldsymbol{\mu}} = \text{ESPRIT}(\mathbf{U}[:,1:L_o]), \in \mathbb{R}^{L_o} \quad (10)$$

where $\hat{\boldsymbol{\mu}}$ is the output of ESPRIT. Here, we assume that among the L_o number of entries in $\hat{\boldsymbol{\mu}}$, there are L number of parameters that correspond to real parameters, while the remaining $L_o - L$ number of its entries correspond to spurious noise parameters. Now that the parameters-of-interest are estimated, MOS can be performed on the entries of the vector $\hat{\boldsymbol{\mu}}$.

3.2 Order Selection

In this section, the proposed MOS method, i.e., Angular Separation between the Reconstructed Eigenvectors and the Noise subspace

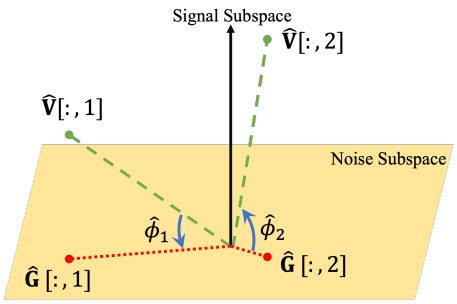

Fig. 1: Intuitive demonstration of ASREN. Horizontal plane and vertical axes represent the noise and signal subspaces, respectively. The reconstructed vectors, $\hat{\mathbf{V}}[:,1]$ and $\hat{\mathbf{V}}[:,2]$, are drawn with dashed lines, while their projections on the noise subspace, $\hat{\mathbf{G}}[:,1]$ and $\hat{\mathbf{G}}[:,2]$, are drawn with dotted lines. We propose to use the angle $\hat{\phi}_l$ as the MOS metric. In this example, $\hat{\mathbf{V}}[:,1]$ corresponds to a spurious noise parameter, while $\hat{\mathbf{V}}[:,2]$ is a real parameter.

(ASREN), is explained in detail. First, let us construct the oversized Vandermonde matrix based on the previously obtained $\hat{\boldsymbol{\mu}}$, while assuming that K_3 and the generic normalization factor η, are known

$$\hat{\mathbf{V}} = \begin{pmatrix} 1 & \dots & 1 \\ \omega(\hat{\mu}_1\eta) & \dots & \omega(\hat{\mu}_{L_o}\eta) \\ \vdots & \ddots & \dots \\ \omega\big((K_3-1)\hat{\mu}_1\eta\big) & \dots & \omega\big((K_3-1)\hat{\mu}_{L_o}\eta\big) \end{pmatrix} \in \mathbb{C}^{K_3\times L_o}. \tag{11}$$

In the meantime, we remind that the remaining eigenvectors in $\mathbf{U}$, i.e., the last $K_3 - L_o + 1$ columns of $\mathbf{U}_e$, such that $\mathbf{U}_e = \mathbf{U}[:, L_o+1:K_3]$, span the noise subspace of its parent matrix, e.g., $\boldsymbol{\mathcal{H}}$. Therefore, one can construct the noise projection matrix and project the reconstructed vectors onto the noise subspace as follows

$$\hat{\mathbf{G}} = \mathbf{U}_e\mathbf{U}_e^*\hat{\mathbf{V}}, \in \mathbb{C}^{K_3\times L_o}. \tag{12}$$

Here, the columns of $\hat{\mathbf{G}}$ correspond to the projections of the columns of $\hat{\mathbf{V}}$ on the noise subspace, i.e., their shadows on the noise plane. Thus, the angular separation between the associated columns of these two matrices i.e., $\hat{\mathbf{V}}_o[:,l]$ and $\hat{\mathbf{G}}[:,l]$, holds the information about the estimated parameter $\hat{\mu}_l$: it is either a real parameter or a spurious noise parameter. The intuition behind this MOS method is shown in Fig. 1 and the corresponding angle can be obtained as follows

$$\hat{\phi}_l = \arccos\left(\frac{\hat{\mathbf{V}}[:,l]\hat{\mathbf{G}}[:,l]^T}{\left\|\hat{\mathbf{V}}[:,l]\right\| . \left\|\hat{\mathbf{G}}[:,l]\right\|}\right)$$

where $\hat{\phi}_l$ is the lth entry in the vector $\hat{\boldsymbol{\phi}}$. Furthermore, let us define the decision vector $\mathbf{d} \in \mathbb{R}^{L_o}$, whose entries are obtained as follows

$$d_l = \begin{cases} l, & \hat{\phi}_l > \mathcal{T} \\ 0, & \text{elsewhere} \end{cases}, l = 1 \dots L_o \tag{13}$$

where the angle between the reconstructed vector and the noise subspace is compared against a detection threshold $\mathcal{T}$. If this angle is bigger than the threshold, the corresponding parameter is marked as a true and real parameter and its index is kept. Otherwise, the estimated parameter will be discarded. The entries in the decision vector $\mathbf{d}$ allows us to select the corresponding entries in $\hat{\boldsymbol{\mu}}$ and columns from $\hat{\mathbf{V}}$, such that

$$\tilde{\boldsymbol{\mu}} = \hat{\boldsymbol{\mu}}[\mathbf{d}], \in \mathbb{R}^{\tilde{L}} \tag{14}$$

$$\tilde{\mathbf{V}} = \hat{\mathbf{V}}[1:K_1, \mathbf{d}], \in \mathbb{C}^{K_1\times\tilde{L}} \tag{15}$$

where entries in $\tilde{\boldsymbol{\mu}}$ contain the selected parameters, and its size $\tilde{L}$ is the number of selected parameters that satisfies (13) i.e., the estimated size of the signal subspace. Here, the term true refers to the actual parameters, which we don't have access to, while selected parameters correspond to the estimation and decision output. Moreover, the columns of $\tilde{\mathbf{V}}$ correspond to the constructed vectors associated with the entries in $\tilde{\boldsymbol{\mu}}$. Since the Vandermonde structured matrix is extracted from the measurement matrix $\hat{\mathbf{Y}}$, one can also estimate the source matrix $\hat{\mathbf{B}}$ through pseudo-inverse: $\tilde{\mathbf{B}} = \tilde{\mathbf{V}}^+\hat{\mathbf{Y}}, \in \mathbb{C}^{\tilde{L}\times K_2}$.

Finally, we define RIVES() as the function whose input-output relation is given as

$$\tilde{\boldsymbol{\mu}},\ \tilde{\mathbf{B}} = \text{RIVES}(\hat{\mathbf{Y}}, L_o, \eta) \tag{16}$$

4 Estimation of the Radar Parameters with RIVES

The matrix model given in (5) contains three layers of matrices: range, AoA and speed, two of which are in Vandermonde form. By using RIVES, we successively obtain these matrices in the given order. We remind that M number of OFDM symbols are needed to estimate the Doppler frequencies. Thus, whenever there is an available OFDM symbol for channel estimation, it is first used to estimate range and AoA information. By keeping track of the index m, the speed/Doppler-frequency can be estimated when there are sufficient number of samples. This flexibility brings a crucial advantage against the unpredictable availability of Wi-Fi frames.

4.1 Range and AoA Estimation

Let us start by defining the first layer where the delay matrix and its related source matrix is obtained through RIVES. For the sake of clarity, we continue our derivations without using the slow-time index (m). The range processing by RIVES is defined as

$$\tilde{\boldsymbol{\tau}},\ \tilde{\mathbf{A}}\tilde{\boldsymbol{\Theta}}^T = \text{RIVES}\left(\hat{\mathbf{H}}, L_o, \frac{2\pi}{QT}\right). \tag{17}$$

Here, the entries in $\tilde{\boldsymbol{\tau}} \in \mathbb{R}^{\tilde{L}_\tau}$ correspond to the unique estimated propagation delays associated with the columns of $\mathbf{D}$, and $\tilde{L}_\tau$ is the number of estimated unique delays.

Since the delay matrix is obtained, one can use RIVES to estimate the AoA parameters per estimated unique range, i.e., for each column of $\hat{\mathbf{D}}$ such that $\hat{\mathbf{D}}[:,i], i = 1, \dots, \tilde{L}_\tau$, as follows

$$\tilde{\boldsymbol{\theta}}^{(\tilde{\tau}_i)},\ \tilde{\mathbf{A}}^{(\tilde{\tau}_i)} = \text{RIVES}\left(\hat{\mathbf{B}}_D[:,i], L_o, \pi\right) \tag{18}$$

where $\hat{\mathbf{B}}_D = \tilde{\mathbf{A}}\tilde{\boldsymbol{\Theta}}^T$. Thus, the entries in $\tilde{\boldsymbol{\theta}}^{(\tilde{\tau}_i)} \in \mathbb{R}^{\tilde{L}_\theta}$ correspond to the AoA estimations with $\tilde{L}_\theta$ being the number of unique AoA values at unique range $\tilde{\tau}_i$. Similarly, $\tilde{\mathbf{A}}^{(\tilde{\tau}_i)}$ contains only the Doppler phases of the paths at τ_i. Here, another possibility is to use the entire matrix $\hat{\mathbf{B}}_D$ for AoA estimation during the second layer. However, this implicitly means that each path in the wireless channel has a unique pair of τ and θ values, i.e., any two paths cannot exist at the same distance and AoA, which is an unlikely assumption. Thus, by feeding individual columns of $\hat{\mathbf{B}}_D$ for AoA processing, we guarantee that for each unique range, all the AoAs that exist at that range are estimated.

4.2 Speed Estimation

The successive estimation stages given in (17) and (18) are based on a single OFDM symbol, measured at time instant m. Once these two stages are finalized, RIVES outputs the following matrix $\tilde{\mathbf{A}}^{(\tilde{\tau}_i)}(m) \in \mathbb{C}^{\tilde{L}_\theta\times\tilde{L}_\theta}$ whose diagonal entries correspond to the Doppler phases of each path at range τ_i and time instant m. Therefore, one-to-one association between the propagation delay and AoA values are still maintained. Once M number of measurements are

obtained, one can construct Doppler phase matrix at AoA $\tilde{\theta}_j^{(\tilde{\tau}_i)}$, i.e., per entry of $\tilde{\boldsymbol{\theta}}^{(\tau_i)}$, such as

$$\boldsymbol{\mathcal{A}}^{\tilde{\theta}_j^{(\tilde{\tau}_i)}} = \boldsymbol{\mathcal{A}}^{(\tilde{\tau}_i,\tilde{\theta}_j)} = \begin{pmatrix} \boldsymbol{\Lambda}(1)[\mathbf{k}] \\ \boldsymbol{\Lambda}(2)[\mathbf{k}] \\ \vdots \\ \boldsymbol{\Lambda}(M)[\mathbf{k}] \end{pmatrix} \tag{19}$$

where $\mathbf{k}$ is a vector whose entries index the Doppler phase terms present only at $\tilde{\tau}_i$ and $\tilde{\theta}_j$. Moreover, $\boldsymbol{\Lambda}(m)$ is a row vector composed of the diagonal entries in $\mathbf{A}(m)$. Since the Vandermonde structure is still present, and the one-to-one association is maintained, RIVES can be used to estimate the Doppler frequencies in $\boldsymbol{\mathcal{A}}^{(\tilde{\tau}_i,\tilde{\theta}_j)}$ as follows

$$\tilde{\mathbf{f}}^{(\tilde{\tau}_i,\tilde{\theta}_j)}, \sigma_Z^2\mathbf{I} = \text{RIVES}\big(\boldsymbol{\mathcal{A}}^{(\tilde{\tau}_i,\tilde{\theta}_j)}, L_o, T_f\big) \tag{20}$$

where σ_Z^2 corresponds to the variance of the noise. The entries in $\tilde{\mathbf{f}}^{(\tilde{\tau}_i,\tilde{\theta}_j)}$ correspond to the estimated Doppler frequencies at unique range $\tilde{\tau}_i$ and $\tilde{\theta}_j$. Therefore, after 3 successive layers of RIVES, we obtain sets of delay, AoA and Doppler frequency estimations.

4.3 Recursive Implementation of RIVES

In this section, the implementation of RIVES is explained in more detail. Since it is used in all layers of the parameter estimation, with the only difference being the generic normalization factor, it can be implemented as a recursive function. In other words, when RIVES is recursively called, a set of parameters estimated in the previous layer is used to estimate the parameters in the next layer. The block diagram shown in Fig. 2 explains this recursive implementation of RIVES which can be summarized as follows:

1. Based on the CTF matrix $\hat{\mathbf{H}}(m)$ measured at time instant m, unique path delays in the wireless channel are estimated, i.e., entries in $\tilde{\boldsymbol{\tau}} \in \mathbb{R}^{\tilde{L}_\tau}$. Through the LS, associated subspaces are extracted for further processing.
2. For any given unique path delay $\tilde{\tau}_i,\ i \in [1, \tilde{L}_\tau]$, the unique AoA parameters are estimated. This step is repeated $\tilde{L}_\tau$ times (or executed in parallel) such that all the path angles at range $\tilde{\tau}_i$ are estimated, which corresponds to the entries in $\tilde{\boldsymbol{\theta}}^{(\tilde{\tau}_i)}$.
3. Once the steps 1 and 2 are repeated M times, the Doppler phases are isolated for each path delay and AoA. Then, the matrix $\boldsymbol{\mathcal{A}}^{(\tilde{\tau}_i,\tilde{\theta}_j)}$ is formed which is used to estimate the Doppler frequencies present at $\tilde{\tau}_i$ and $\tilde{\theta}_j$.

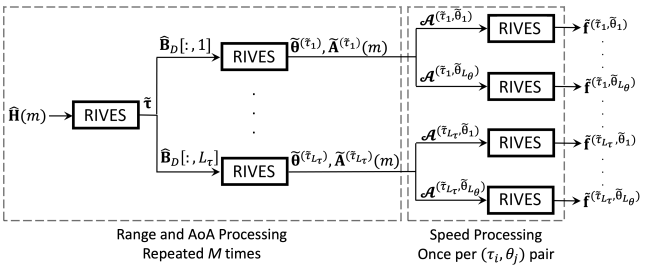

Fig. 2: Recursive implementation of RIVES allows successive subspace isolation for parameter estimation.

In essence, RIVES runs once to estimate the unique ranges and isolate the AoA subspace. Then, for each estimated unique range, RIVES will run again to estimate the unique AoA values from their isolated subspaces. Finally, for each unique range-AoA pair, RIVES will be used to estimate the speed of the corresponding target. Therefore, the number of times that RIVES will run completely depends on the number of targets, as well as their unique range/AoA/speed values.

Thanks to the left-right (or equivalently top-down) branching, one-by-one association between the estimated parameters are maintained. One may argue that jointly estimating all the parameters of $\hat{\mathbf{H}}$ is more robust and -depending on the context- relatively more straight forward. However, in multipath rich environments, such as indoor wireless channels, recursive extraction of subspaces provides additional advantages. First, estimation of the size of an isolated subspace is much more ideal compared to the estimation of the total number of paths directly from $\hat{\mathbf{H}}$, i.e., estimating P in (1). Simply put, the estimation of the size of the entire space depends on minimizing (or maximizing) a cost function or an information criteria [17]. However, due to the richness of MPCs, channel statistics drastically vary which makes it difficult to find a cost function that fits every scenario. In contrast, RIVES independently estimates the size of each subspace based on the orthogonality between signal and noise subspaces. Second, jointly estimating the channel parameters directly from $\hat{\mathbf{H}}$ requires a solution space where a global minima/maxima can be found. However, such methods are known to stuck at a local minima/maxima, especially if the number of paths is high and/or incorrectly estimated [33]. Moreover, highly varying and independent statistics of diffuse MPCs yield a mismatch between the models and real-life channels. In contrast, RIVES relies only on the measured data itself to separate the true paths from the spurious noise paths. Under semi-ideal conditions where there is only thermal noise, RIVES outperforms other algorithms as shown in Section 5 and Section 6.

5 Numerical Results

In this section, the accuracy and reliability of RIVES are numerically assessed under different conditions. The statistical consistency of ASREN and the accuracy of the spectral parameter estimation determine the overall reliability and accuracy of RIVES. Thus, the two stages are separately analyzed. Table 2 summarizes the standard-compliant parameters used in simulations.

Table 2 Summary of the simulation parameters

Symbol	Parameter	Value	Unit
Q	Number of subcarriers	64, 256, 1024	
M	Number of OFDM symbols	60, ..., 200	
N	Number of antennas at Rx	4, 8	
B	Bandwidth	20, 80	MHz
f_c	Carrier frequency	2.45	GHz
σ_{human}	RCS of human targets	-4	dBsm
T_f	Slow-time sampling rate	0.01, 0.1, 1	ms

5.1 Model Order Selection with ASREN

In Fig. 3, values of the MOS metric are provided as a function of the SNR of a single target over 10000 realizations. The entries of $\tilde{\boldsymbol{\phi}}$ in (13) corresponding to only the real and the strongest noise targets are shown. First, the mean of the metric increases with SNR, while its variance decreases in all dimensions. Second, the range layer shows slightly better performance compared to other layers since the noise samples are better averaged when the number of available samples is larger, i.e., $M, N < Q$. Third, the strongest metric corresponding to a spurious noise target, and its variance, remain constant for all layers, regardless of the target SNR. This is expected since the noise power is mainly a function of the signal bandwidth and system temperature. Since the differences between the metrics corresponding to the real target and the noise are sufficiently high, a Range Aware Threshold (RAT) can be drawn whose purpose is to select the appropriate threshold for ASREN at any layer. Furthermore, $\mathcal{T}$ defined in (13) corresponds to a single point on the RAT curve. Since the difference between noise and target metrics is not sufficiently high when SNR is below -3 dB, there is an intrinsic limit on the minimum

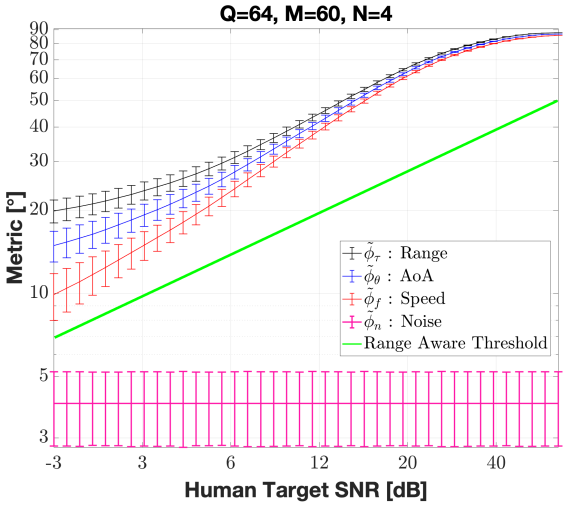

Fig. 3: Mean and variance of the metric corresponding to the real parameters in all dimensions ($\hat{\phi}_\tau$, $\hat{\phi}_\theta$ and $\hat{\phi}_f$) and the strongest noise parameter (ϕ_n), estimated by ASREN as a function of SNR.

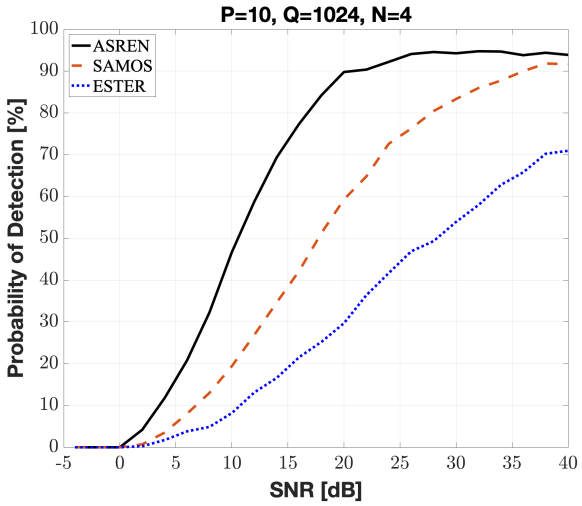

Fig. 4: Comparison between ASREN, ESTER [20] and SAMOS [21] in terms of probability of target detection as a function of the SNR.

SNR that RIVES can reliably operate, which is a potential drawback. However, depending on the scenario, SNR can reach to relatively high values, especially when indoor conditions are considered.

In Fig. 4, the statistical performance of ASREN is compared with two other techniques, namely SAMOS and ESTER. In [21] and [20], the Probability of Detection (PD) performance of SAMOS and ESTER are studied as a function of SNR for only two and three uncorrelated sources, i.e., $P = 2, 3$. From a communication perspective, such low values might be valid assumptions. However, in the radar (or WS) context, $P = 3$ essentially means that there are only 3 targets in the environment, which is not realistic at all. In order to show the impact of P, and the true power of ASREN, we consider 10 human targets, i.e., $P = 10$. Each human target is randomly placed on the 3D range/AoA/speed grid with a minimum separation of 1 meter, 2 degrees and 0.4 m/s, respectively. The probability of detecting all the targets is computed after 10000 realizations per SNR. First of all, when SNR is below 0 dB, none of the methods work when there are 10 targets in the environment, simply because entries in the corresponding SCMs (or Hankel matrix for ASREN) do not contain sufficient information to separate all the targets. Once the SNR is increased, ASREN is the first algorithm that starts to show an improved performance, followed by SAMOS and ESTER,

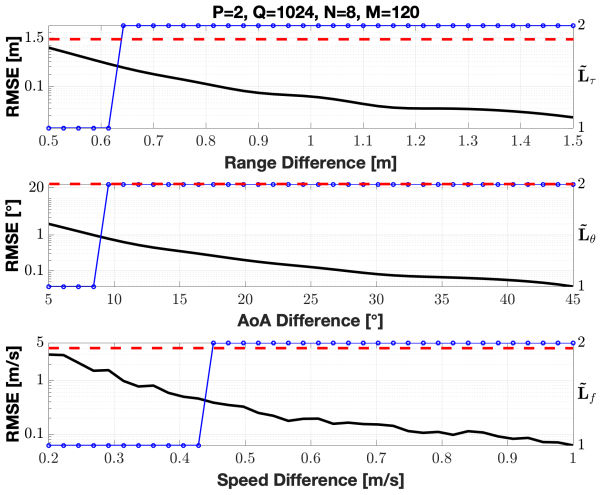

Fig. 5: Estimation accuracy of RIVES as a function of the difference in range, AoA and speed between two human targets. Left and right vertical axes show the overall estimation accuracy of RIVES and the output of ASREN, i.e., estimated number of targets, respectively. Solid (black) and dashed (red) lines correspond to the RMSE of RIVES and FFT-based processing, respectively. Blue line with markers correspond to the output of ASREN.

respectively. Moreover, ASREN reaches a PD ceiling at around 95% when SNR is 25 dB, while SAMOS needs 40 dB of SNR to reach the same error ceiling.

5.2 *Estimation Accuracy*

Any given set of closely located paths (whether in range, AoA or speed dimensions) may not be resolved separately. There are two underlying reasons. First, the noise at the receiver which distorts the characteristics of the signal subspace and makes it difficult for ASREN to resolve them separately. This particular problem is addressed in [22] by studying the Cramer-Rao Lower Bound of closely-spaced paths. Second, we assume that each path is specular in our simulations, i.e., there is only a single Dirac Delta function associated with any given target. However, in reality, any given major path can be surrounded by other minor paths also known as diffuse paths [34] [35]. In this case, depending on the diffuse characteristic of each path, one may hide the other even though they are not closely spaced.

In Fig. 5, the estimation accuracy of RIVES is shown in terms of Root Mean Square Error (RMSE). In this scenario, RMSE is computed as a function of the range, AoA and speed difference between two targets, shown in the first, second and last rows, respectively, while the closest human target is placed at 20 meters distance. Thanks to the parametric super-resolution principles, RIVES provides higher accuracy than the FFT-based resolution in all cases. When the difference between two targets is not large enough in any given dimension, ASREN detects only a single target since the SNR is not sufficient enough to resolve the two targets. In other words, the eigenvalue decomposition of the corresponding Hankel matrix yields only a single eigenvector that spans the combined subspace of the two targets. Therefore, RIVES outputs only a single estimation, corresponding to the combined range/AoA/Speed of the two targets. Once the difference between targets is large enough for the given SNR, ASREN can resolve both targets. Therefore, the overall estimation accuracy is maintained.

6 Experimental Results

In this section, we provide experimental results by applying RIVES to real-life measurements obtained with SDRs. In Fig. 6, the experimental setup and the corresponding measurement scenario are

shown. The measurements took place in a 6m $\times$ 20m corridor, and 9 snapshots were obtained, each separated by 0.5 seconds. Table 3 summarizes the parameters used in our experiments.

In Fig. 7, the estimated target positions are plotted for all snapshots. To do so, the polar coordinates at the output of RIVES (i.e., range and AoA estimations) are converted into Cartesian coordinates, and any speed detection between -0.5 and 0.5 m/s are discarded as they are assumed to be a part of the static clutter. First of all, even though there are two human targets in the environment, RIVES always detects more targets at each snapshot. These additional detections correspond to either limbs of the human targets or radio waves reflected from the walls, also known as ghost targets which is a common problem in multipath-rich environments. In order to deal with indoor ghost targets, multiple radar receivers can be deployed in multi-static configuration [38] [39] [40], or the tracking algorithms can be adjusted accordingly [41] since the tracks followed by ghost targets are much less consistent compared to the tracks followed by real targets.

In order to assess the performance of RIVES, simple tracks are instantiated by using the velocity gating and without making any tracking-related predictions i.e., by using only the measurements. Over 9 snapshots, 5 tracks are instantiated which can be grouped into three categories. First, two temporary tracks are located at the top-left of the figure. Due to their inconsistency, velocity gating removes these tracks after the sixth snapshot. Second, a more consistent ghost target yields a track that appears on all snapshots (on the right side of the figure). However, as mentioned earlier, this is a typical issue in MPC rich environments. Third, the two tracks correspond to the real targets (located in the middle of the figure) and closely follow the ground truth. Notice that, as the distance of real targets increases, the corresponding SNR decrease, yielding relatively larger position estimation errors.

One may argue that all the additional detections could correspond to spurious noise targets which are not discarded by ASREN. In order to check that ASREN only keeps echoes from real targets and not noise, the amplitudes of detected paths from the previous experiment are illustrated as a function of path distance in Fig. 8. Notice that the amplitude of each path coincides with typical path loss models, following a log-like decreasing pattern. If there was a spurious noise target, there would have been outliers in the amplitude data. Therefore, the detected MPCs are either real or ghost targets, but certainly not spurious noise targets.

Finally, in Fig. 9 the position and speed estimation errors of the real targets are provided for the same scenario while the wireless channel is measured over 9 snapshots. First, the position and speed errors increase as a function of the target range, since estimation errors are inversely proportional to the SNR. With RIVES, the average position error of both targets is less than 0.3 meters, and the average speed error is below 0.4 m/s. When the targets are around a similar range, their position and speed estimation accuracy are also similar which shows the consistency of RIVES. With the FFT-based processing, the estimation accuracy is directly limited by the system resolution, yielding roughly 0.5m and 0.52m/s larger position and speed errors, respectively. Moreover, the estimation accuracy shown in Fig. 5 cannot be achieved in real-life. One source of this problem is the impact of hardware non-idealities [42], e.g. Phase Noise, on the accuracy of subspace-based estimation techniques [43] [44].

Table 3 Summary of the parameters used in experiments.

Symbol	Parameter	Value	Unit
Q	Number of subcarriers	1024	
M	Number of OFDM symbols	120	
N	Number of antennas at Rx	4	
B	Bandwidth	80	MHz
f_c	Carrier frequency	2.45	GHz
P_{tx}	SDR Tx power	20	dBm
G_{rx}	SDR Rx gain	20	dB
T_f	Slow-time sampling rate	0.01	ms
ΔT	Snapshot sampling rate	0.5	s

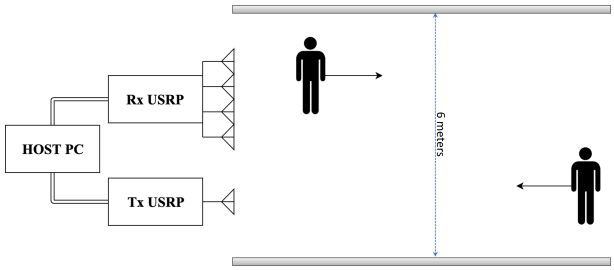

Fig. 6: The experimental setup from top-view. Tx/Rx antennas are separated by absorbers. The width of the corridor emulates a typical living room, and its length is sufficiently high to produce different SNR values. USRP X310s are used as SDR devices.

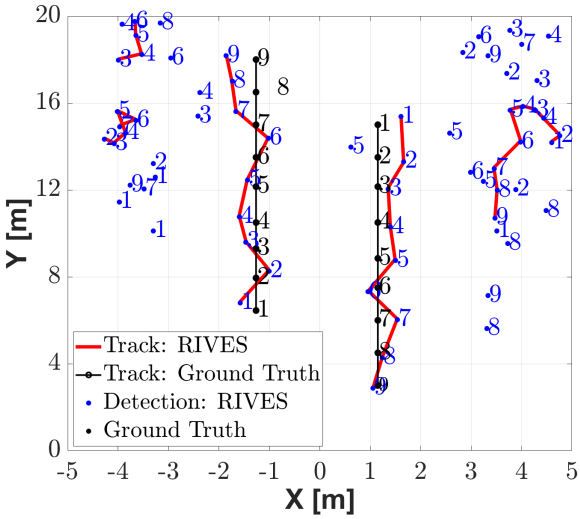

Fig. 7: Output of RIVES over all snapshots. The markers and the numbers next them indicate the position of the estimated MPCs and the index of the snapshots, respectively. Tracks are instantiated with simple velocity gating: the estimated velocity of an MPC is multiplied with ΔT, which yields a circle of possible future positions. If there is an MPC that falls inside this circle in the next snapshot, the two MPCs are connected and a track is instantiated [36] [37].

7 Conclusion

In this work, we proposed a new super-resolution algorithm structure, RIVES, which combines a novel MOS method, ASREN, with the well-known super-resolution algorithm ESPRIT. In essence, RIVES is an algorithm that estimates the propagation distance, AoA and Doppler frequency of any given path. In order to keep the discussion simple, we have assumed a quasi-monostatic geometry, e.g., the range of a target is given as the half of its estimated propagation distance due to two-way propagation. Thus, in a bistatic scenario, RIVES can still successfully estimate the bistatic range/AoA/speed of the targets. However, an additional processing will be required to estimate the true range/AoA/speed of the targets, as it is the case in conventional bistatic radar processing schemes.

Furthermore, RIVES is specifically designed to deal with MPC rich environments by recursively isolating each measurement dimension, and estimating the spectral parameters in each dimension. Our numerical and experimental analysis show that RIVES, together with ASREN, achieve sufficient estimation accuracy for indoor target detection and tracking. Even for closely spaced targets, RIVES is shown to be accurate and reliable enough to detect and track multiple human targets. However, some of the ghost tracks can be removed by a simple tracking method with velocity gating, more consistent ghost tracks still remain to be an issue.

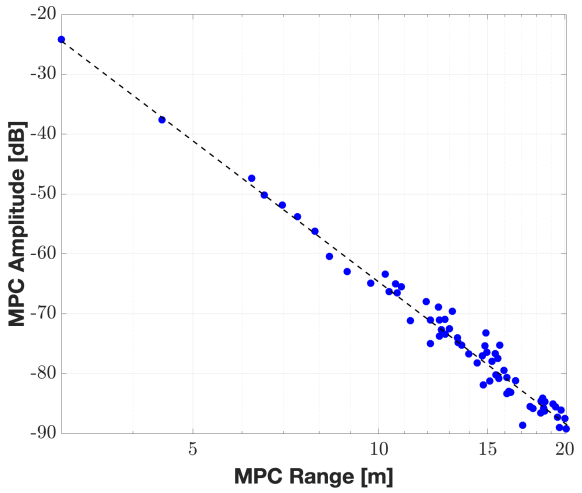

Fig. 8: The dots illustrate the MPC amplitudes as a function of the range. The solid line corresponds to a fitted path loss model. Having no outliers shows that ASREN kept only the real MPCs, including the ghost targets.

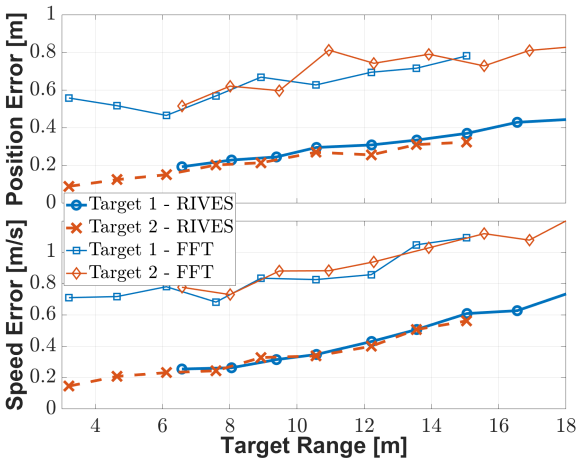

Fig. 9: The radar performance over 9 successive measurements. Position error is computed by converting range and AoA estimates to XY coordinates.

8 References

1 Yildirim, H.C., Storrer, L., Eechkhaute, M.V., Desset, C., Louveaux, J., Horlin, F. 'Passive radar based on 802.11ac signals for indoor object detection'. In: 2019 16th European Radar Conference (EuRAD). (, 2019. pp. 153–156

2 Li, W., Piechocki, R.J., Woodbridge, K., Tang, C., Chetty, K.: 'Passive wifi radar for human sensing using a stand-alone access point', *IEEE Transactions on Geoscience and Remote Sensing*, 2020, **59**, (3), pp. 1986–1998

3 Richards, M.A., Scheer, J., Holm, W.A., Melvin, W.L.: 'Principles of modern radar', , 2010,

4 IEEE. 'Enabling new applications of wlan technology: Wlan sensing'. (, 2021. Available from: https://beyondstandards.ieee.org/ieee-802-11bf-aims-to-enable-a-new-application-of-wlan-technology-wlan-sensing/

5 Ma, Y., Zhou, G., Wang, S.: 'Wifi sensing with channel state information: A survey', *ACM Computing Surveys (CSUR)*, 2019, **52**, (3), pp. 1–36

6 Wallace, J.W., Jensen, M.A.: 'Modeling the indoor mimo wireless channel', *IEEE Transactions on Antennas and Propagation*, 2002, **50**, (5), pp. 591–599

7 Wallace, J.W., Jensen, M.A., Swindlehurst, A.L., Jeffs, B.D.: 'Experimental characterization of the mimo wireless channel: data acquisition and analysis', *IEEE Transactions on Wireless Communications*, 2003, **2**, (2), pp. 335–343

8 Kermoal, J.P., Mogensen, P.E., Jensen, S.H., Andersen, J.B., Frederiksen, F., Sorensen, T.B., et al. 'Experimental investigation of multipath richness for multi-element transmit and receive antenna arrays'. In: VTC2000-Spring. 2000 IEEE 51st Vehicular Technology Conference Proceedings (Cat. No.00CH37026). vol. 3. (, 2000. pp. 2004–2008 vol.3

9 Networks, A.. 'Wi-fi 6: 802.11ax'. (, . accessed: 2010-09-30. https://www.arubanetworks.com/assets/wp/WP_802.11AX.pdf

10 Stoica, P., Moses, R.L., et al.: 'Spectral analysis of signals', , 2005,

11 Schmidt, R.: 'Multiple emitter location and signal parameter estimation', *IEEE Transactions on Antennas and Propagation*, 1986, **34**, (3), pp. 276–280

12 Roy, R., Kailath, T.: 'Esprit-estimation of signal parameters via rotational invariance techniques', *IEEE Transactions on acoustics, speech, and signal processing*, 1989, **37**, (7), pp. 984–995

13 Eriksson, A., Stoica, P., Söderström, T. 'Second-order properties of music and esprit estimates of sinusoidal frequencies in high snr scenarios'. In: IEE Proceedings F (Radar and Signal Processing). vol. 140. (IET, 1993. pp. 266–272

14 Gu, J.F., Moghaddasi, J., Wu, K. 'Delay and doppler shift estimation for ofdm-based radar-radio (radcom) system'. In: 2015 IEEE international wireless symposium (IWS 2015). (IEEE, 2015. pp. 1–4

15 Nguyen, D.H., Heath, R.W. 'Delay and doppler processing for multi-target detection with ieee 802.11 ofdm signaling'. In: 2017 IEEE International Conference on Acoustics, Speech and Signal Processing (ICASSP). (IEEE, 2017. pp. 3414–3418

16 Belouchrani, A., Amin, M.G.: 'Blind source separation based on time-frequency signal representations', *IEEE Transactions on Signal Processing*, 1998, **46**, (11), pp. 2888–2897

17 Stoica, P., Selen, Y.: 'Model-order selection: a review of information criterion rules', *IEEE Signal Processing Magazine*, 2004, **21**, (4), pp. 36–47

18 Carotenuto, V., De.Maio, A., Orlando, D., Stoica, P.: 'Model order selection rules for covariance structure classification in radar', *IEEE Transactions on Signal Processing*, 2017, **65**, (20), pp. 5305–5317

19 Radoi, E., Quinquis, A.: 'A new method for estimating the number of harmonic components in noise with application in high resolution radar', *EURASIP Journal on Advances in Signal Processing*, 2004, **2004**, (8), pp. 1–12

20 Badeau, R., David, B., Richard, G. 'Selecting the modeling order for the esprit high resolution method: an alternative approach'. In: 2004 IEEE International Conference on Acoustics, Speech, and Signal Processing. vol. 2. (IEEE, 2004. pp. ii–1025

21 Papy, J.M., De.Lathauwer, L., Van.Huffel, S.: 'A shift invariance-based order-selection technique for exponential data modelling', *IEEE signal processing letters*, 2007, **14**, (7), pp. 473–476

22 Yildirim, H.C., Determe, J.F., Storrer, L.e.a.: 'Super resolution passive radars based on 802.11ax wi-fi signals for human movement detection', *IET Radar, Sonar & Navigation*, 2021, **15**, (4), pp. 323–339

23 Yang, Z., Xie, L., Stoica, P.: 'Vandermonde decomposition of multilevel toeplitz matrices with application to multidimensional super-resolution', *IEEE Transactions on Information Theory*, 2016, **62**, (6), pp. 3685–3701

24 Vandersmissen, B., Knudde, N., Jalalvand, A., Couckuyt, I., Bourdoux, A., De.Neve, W., et al.: 'Indoor person identification using a low-power fmcw radar', *IEEE Transactions on Geoscience and Remote Sensing*, 2018, **56**, (7), pp. 3941–3952

25 Bauduin, M., Bourdoux, A. 'Mixed-signal transmitter leakage cancellation for pmcw mimo radar'. In: 2018 15th European Radar Conference (EuRAD). (IEEE, 2018. pp. 293–296

26 Bourdoux, A., Bauduin, M. 'Pmcw waveform cross-correlation characterization and interference mitigation'. In: 2020 17th European Radar Conference (EuRAD). (IEEE, 2021. pp. 164–167

27 Cho, Y.S., Kim, J., Yang, W.Y., Kang, C.G.: 'MIMO-OFDM wireless communications with MATLAB'. (John Wiley & Sons, 2010)

28 Yildirim, H.C., Louveaux, J., Doncker, P.D., Horlin, F. 'Impact of interference on ofdm based radars'. In: 2020 IEEE 91st Vehicular Technology Conference (VTC2020-Spring). (, 2020. pp. 1–5

29 Qi, L.: 'Hankel tensors: Associated hankel matrices and vandermonde decomposition', *arXiv preprint arXiv:13105470*, 2013,

30 Boley, D.L., Luk, F.T., Vandevoorde, D.: 'Vandermonde factorization of a hankel matrix', *Scientific computing*, 1997, pp. 27–39

31 Shan, T.J., Wax, M., Kailath, T.: 'On spatial smoothing for direction-of-arrival estimation of coherent signals', *IEEE Transactions on Acoustics, Speech, and Signal Processing*, 1985, **33**, (4), pp. 806–811

32 Pillai, S.U., Kwon, B.H.: 'Forward/backward spatial smoothing techniques for coherent signal identification', *IEEE Transactions on Acoustics, Speech, and Signal Processing*, 1989, **37**, (1), pp. 8–15

33 Jin, C., Zhang, Y., Balakrishnan, S., Wainwright, M.J., Jordan, M.I. 'Local maxima in the likelihood of gaussian mixture models: Structural results and algorithmic consequences'. In: Lee, D., Sugiyama, M., Luxburg, U., Guyon, I., Garnett, R., editors. Advances in Neural Information Processing Systems. vol. 29. (Curran Associates, Inc., 2016. Available from: https://proceedings.neurips.cc/paper/2016/file/3875115bacc48cca24ac51ee4b0e7975-Paper.pdf

34 Quitin, F., Oestges, C., Horlin, F., De.Doncker, P. 'Diffuse multipath component characterization for indoor mimo channels'. In: Proceedings of the Fourth European Conference on Antennas and Propagation. (, 2010. pp. 1–5

35 Wen, F., Kulmer, J., Witrisal, K., Wymeersch, H.: '5g positioning and mapping with diffuse multipath', *IEEE Transactions on Wireless Communications*, 2021, **20**, (2), pp. 1164–1174

36 Yeom, S.W., Kirubarajan, T., Bar.Shalom, Y.: 'Track segment association, fine-step imm and initialization with doppler for improved track performance', *IEEE transactions on aerospace and electronic systems*, 2004, **40**, (1), pp. 293–309

37 Wang, X., Musicki, D., Ellem, R., Fletcher, F.: 'Efficient and enhanced multi-target tracking with doppler measurements', *IEEE Transactions on Aerospace and Electronic Systems*, 2009, **45**, (4), pp. 1400–1417

38 Copa, E.I.P., Aziz, K., Rykunov, M., De.Greef, E., Bourdoux, A., Horlin, F. 'Radar fusion for multipath mitigation in indoor environments'. In: 2020 IEEE Radar Conference (RadarConf20). (, 2020. pp. 1–5

39 Feng, R., De.Greef, E., Rykunov, M., Sahli, H., Pollin, S., Bourdoux, A.: 'Multipath ghost recognition for indoor mimo radar', *IEEE Transactions on Geoscience and Remote Sensing*, 2021, pp. 1–10
40 Zhang, Y.D., Himed, B. 'Moving target parameter estimation and sfn ghost rejection in multistatic passive radar'. In: 2013 IEEE Radar Conference (RadarCon13). (IEEE, 2013. pp. 1–5
41 Ryu, I.h., Won, I., Kwon, J.: 'Detecting ghost targets using multilayer perceptron in multiple-target tracking', *Symmetry*, 2018, **10**, (1), pp. 16
42 Horlin, F., Bourdoux, A.: 'Digital compensation for analog front-ends: a new approach to wireless transceiver design'. (John Wiley & Sons, 2008)
43 Qiu, J., Kandeepan, S. 'Performance of frequency estimation techniques with phase noise in mm-wave based 5g systems'. In: 2017 Asia Modelling Symposium (AMS). (IEEE, 2017. pp. 170–175
44 Reck, C., Berold, U., Weinzier, J., Schmidt, L. 'Direction of arrival estimation from secondary surveillance radar signals in presence of hardware imperfections'. In: 2008 European Radar Conference. (IEEE, 2008. pp. 252–255